

An upper limit on Gibbs energy dissipation governs cellular metabolism

Bastian Niebel ^{1,2}, Simeon Leupold ^{1,2} and Matthias Heinemann ^{1*}

The principles governing cellular metabolic operation are poorly understood. Because diverse organisms show similar metabolic flux patterns, we hypothesized that a fundamental thermodynamic constraint might shape cellular metabolism. Here, we develop a constraint-based model for *Saccharomyces cerevisiae* with a comprehensive description of biochemical thermodynamics including a Gibbs energy balance. Non-linear regression analyses of quantitative metabolome and physiology data reveal the existence of an upper rate limit for cellular Gibbs energy dissipation. By applying this limit in flux balance analyses with growth maximization as the objective function, our model correctly predicts the physiology and intracellular metabolic fluxes for different glucose uptake rates as well as the maximal growth rate. We find that cells arrange their intracellular metabolic fluxes in such a way that, with increasing glucose uptake rates, they can accomplish optimal growth rates but stay below the critical rate limit on Gibbs energy dissipation. Once all possibilities for intracellular flux redistribution are exhausted, cells reach their maximal growth rate. This principle also holds for *Escherichia coli* and different carbon sources. Our work proposes that metabolic reaction stoichiometry, a limit on the cellular Gibbs energy dissipation rate, and the objective of growth maximization shape metabolism across organisms and conditions.

Key questions in metabolic research are how and why cells organize their metabolism, or their fluxes through the metabolic network, in a particular manner. Such understanding is highly relevant from a fundamental point of view, but also should enable computational methods for metabolic-flux prediction, which are important in biomedicine and biotechnology.

The archetypal question in this context is why many prokaryotic and eukaryotic cells often use an inefficient fermentative metabolism, even under aerobic conditions. Many explanations have been offered for this, including the economics of enzyme production^{1,2}, a ‘make-accumulate-consume’ strategy³, intracellular crowding⁴, limited nutrient transport capacity⁵, and adjustments to growth-dependent requirements^{6,7}. Recently, the integration of proteome allocation constraints in metabolic models has led to predictions in good agreement with experimental data^{8,9}. However, respiration and aerobic fermentation occur in many organisms, including bacteria⁴, fungi³, mammals^{6,7} and plants¹⁰, with fermentation occurring at high glucose uptake rates (GURs) and respiration at low GURs^{7,11}. This led us to wonder whether a fundamental thermodynamic principle governs metabolism, on top of which specific protein allocation constraints evolved. Specifically, we hypothesized that the rate at which cells, as open systems operating far from equilibrium¹², can dissipate Gibbs energy to the extracellular environment¹³ may be limited and that such a limit may constrain metabolic fluxes.

Here, using a constraint-based thermodynamic model of *S. cerevisiae* and non-linear regression analysis of quantitative metabolome and physiology data, we identified an upper limit for the cellular Gibbs energy dissipation rate. When we used this rate limit in flux balance analyses (FBAs) with growth maximization as objective function, we generated correct predictions of metabolic phenotypes under diverse conditions. As we found the same principle to hold in *E. coli*, our work suggests that growth maximization under the constraint of an upper rate limit on Gibbs energy dissipation must have been the general governing principle in shaping

metabolism and its regulation. Furthermore, our work provides an important contribution to current predictive metabolic modelling for fundamental biology, biomedicine and biotechnology.

Results

Development of a combined thermodynamic–stoichiometric model. To test our hypothesis that cellular metabolism is limited by a certain critical rate of Gibbs energy dissipation, we used the yeast *S. cerevisiae* as a model and aimed to estimate cellular Gibbs energy dissipation rates from experimental data using regression analysis (Fig. 1). Specifically, we formulated a combined thermodynamic and stoichiometric metabolic network model, describing cellular metabolic operation through the variables metabolic flux (reaction rate), v , and metabolite concentration, c . The basis of this model is a stoichiometric metabolic network model¹⁴ (Supplementary Methods 1.1 and Supplementary Note 1) that describes 241 metabolic processes (that is, chemical conversions and metabolite transport, *MET*) of primary metabolism and their mitochondrial or cytosolic localization with mass balances for 156 metabolites (Tables 1–5 in Supplementary Data 1) as well as with pH-dependent proton and charge balances (Tables 6 and 7 in Supplementary Data 1). The boundary of the system was defined around the extracellular space and the exchange of matter with the environment was accomplished through 15 exchange processes (*EXG*) (compare Fig. 1).

To this model, we added a Gibbs energy balance stating that the sum of the Gibbs energy dissipation rates of the individual metabolic processes (that is, the total cellular rate of Gibbs energy dissipation, g^{diss}) must equal the sum of the rates at which Gibbs energy is exchanged with the environment (Supplementary Methods 1.2). We defined the rate of Gibbs energy dissipation of a metabolic process as the product of the metabolic flux of the process and its Gibbs energy. The Gibbs energy of a metabolic process, in turn, was made a function of the substrate and product concentrations, the standard Gibbs energy of the reaction and/or the Gibbs energy of the

¹Molecular Systems Biology, Groningen Biomolecular Sciences and Biotechnology Institute, University of Groningen, Groningen, The Netherlands.

²These authors contributed equally: B. Niebel, S. Leupold. *e-mail: m.heinemann@rug.nl

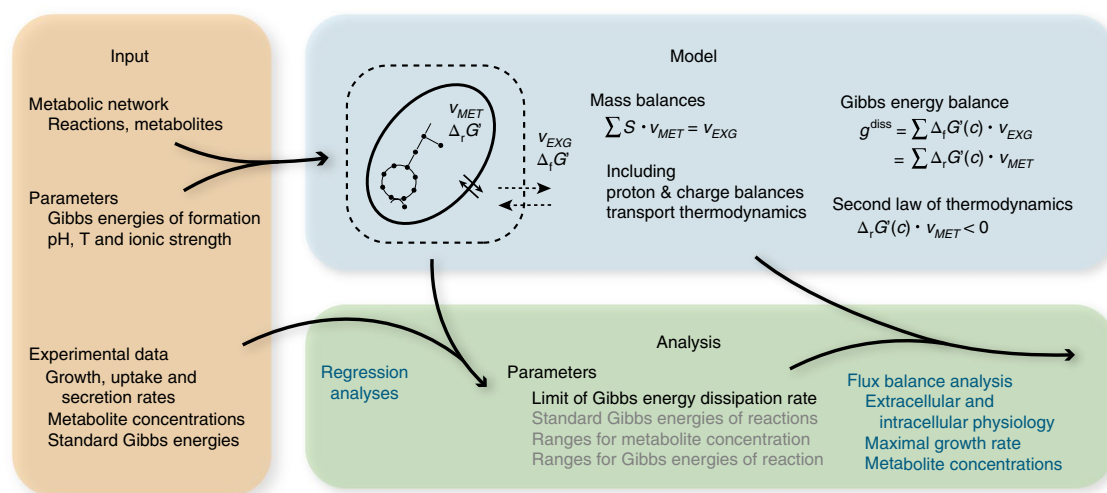


Fig. 1 | Overview of workflow and model. We developed models constrained by thermodynamics and stoichiometry for *S. cerevisiae* and *E. coli*. With these models and experimental data, we performed regression analyses to identify model parameters, including the limiting rate of cellular Gibbs energy dissipation. Using these parameters in FBAs, we then predicted various cellular phenotypes. S is the stoichiometric matrix, v the rates of the respective processes (that is, fluxes), c the metabolite concentrations, $\Delta_r G$ the Gibbs energies of reaction, $\Delta_r G'$ the metabolites' Gibbs formation energies and g^{diss} the Gibbs energy dissipation rates. Subscripted *MET* denotes metabolic processes; subscripted *EXG* denotes exchange processes with the environment. Detailed model descriptions are in Supplementary Methods 1.1–1.6, with *S. cerevisiae*-specific details in Supplementary Note 1 and *E. coli*-specific details in Supplementary Note 2.

metabolite's transmembrane transport¹⁵. We transformed the standard Gibbs energies of the reaction to correspond to the respective compartmental pH values¹⁶ (Supplementary Methods 1.3). Finally, for each metabolic process, we added the second law of thermodynamics stating that the Gibbs energy dissipation rate must be negative for a metabolic process carrying flux (Supplementary Methods 1.4). All metabolic processes in the model were considered reversible.

Limit on the rate of cellular Gibbs energy dissipation. To determine g^{diss} values at different growth conditions, we analysed experimental data with regression analysis using the developed model (Supplementary Fig. 1 and Supplementary Methods 2.1). Specifically, we used physiological data (that is, growth rates, metabolite uptake and excretion rates) and metabolome data of *S. cerevisiae* obtained from eight different glucose-limited chemostat cultures¹⁷. In these cultures, metabolic operation ranged from respiration at low GURs to aerobic fermentation with ethanol production at high GURs. As Gibbs energies estimated with the component contribution method¹⁸ contained uncertainties, and Gibbs energies were not available for all metabolic reactions, we included the available standard Gibbs energies of reaction together with their respective uncertainties as experimental data in the regression.

To enforce one common set of standard Gibbs energies of reaction across all experimental conditions with the same thermodynamic reference state (that is, obeying the first law of thermodynamics, which we enforced by applying the loop law^{19,20}), we performed one large regression across all conditions. In this large-scale multi-step non-linear regression, we estimated for each condition its condition-dependent variables (that is, fluxes and metabolite concentrations), and for all conditions together, a set of condition-independent standard Gibbs energies of reaction with minimal distance to the experimental data.

To prevent overfitting, we employed a parametric bootstrap approach (Supplementary Fig. 2a). The regression and a subsequent variability analysis of the solution space provided us with physiological ranges for the intracellular metabolite concentration and for the Gibbs energies of reaction (that is, the lowest and highest possible

values across all experimental conditions, reflecting the physiological bounds of metabolic operation), which we used to refine the scope of the model (Supplementary Methods 2.2 and Tables 8 and 9 in Supplementary Data 1).

First, we found that the model with its thermodynamic and stoichiometric constraints could be well fitted to all data sets (Supplementary Fig. 2b–d), demonstrating that the developed model can describe the broad range of underlying metabolic operations, ranging from fully respiratory to fermentative conditions. Second, by examining the g^{diss} values determined for the different experimental conditions, we found that g^{diss} first linearly increased with increasing growth rate μ , and then plateaued at μ values $> 0.3 \text{ h}^{-1}$ (Fig. 2). The existence of a plateau above a certain μ suggested, in line with our hypothesis, that there could be an upper rate limit, g^{diss}_{lim} , at which cells can dissipate Gibbs energy, here corresponding to $-3.7 \text{ kJ gram cell dry weight (gCDW)}^{-1} \text{ h}^{-1}$. Because the growth rate at which this limit is reached coincided with the onset of ethanol excretion, we speculated that this limit might cause the switch to fermentation at high GURs.

Accurate predictions of metabolic phenotypes. To test whether such an upper limit on the Gibbs energy dissipation rate might govern metabolic operation, that is, be responsible for the different flux distributions at different GURs, we used FBA, which computes metabolic flux distributions on the basis of a stoichiometric metabolic network model and mathematical optimization using an evolutionary optimization criterion¹⁴. Specifically, we used the objective of growth maximization (that is, identifying the flux distribution that generates the maximal amount of biomass from the available nutrients) to simulate the combined thermodynamic and stoichiometric model, which we additionally constrained by the hypothesized g^{diss}_{lim} (Supplementary Methods 2.2). To solve this nonconvex bilinear optimization problem, we transferred it into a mixed-integer non-linear program, which we then solved using a branch-and-cut global optimization algorithm²¹ (Supplementary Methods 1.5, 1.6 and 2.3).

Previously, it was shown that the objective of growth maximization alone could not predict flux distributions across experimental

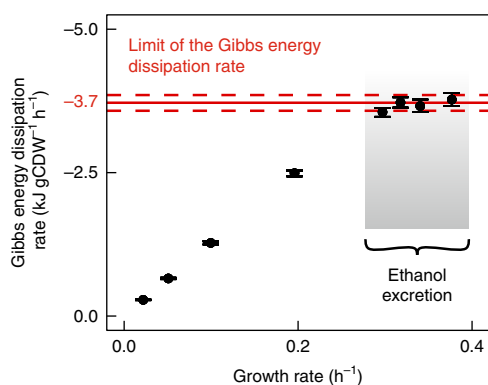


Fig. 2 | Rate of cellular Gibbs energy dissipation does not exceed an upper limit. The median g^{diss} (black dots), determined by regression analysis including a parametric bootstrap ($n = 2,000$) using the model, the physiological and metabolome data¹⁷ and the Gibbs energies from the component contribution method¹⁸, reached an upper limit coinciding with the onset of aerobic fermentation (ethanol excretion). The $g^{\text{diss}}_{\text{lim}}$ was determined from the g^{diss} values at the plateau. The solid red line represents the median of those values and the dashed red lines the 97.5% confidence interval. Although the regression was largely underdetermined (107 degrees of freedom, Supplementary Fig. 2a), g^{diss} could be estimated with high confidence because g^{diss} could in principle already be directly estimated using perfect physiological rate measurements (compare Supplementary Equation 4 in Supplementary Methods 1.2). Error bars represent the 97.5% confidence intervals as determined by the parametric bootstrap ($n = 2,000$).

conditions²². But by using it in combination with the identified upper limit on g^{diss} , we correctly predicted physiologies as observed in glucose-limited chemostat cultures and in glucose batch cultures, solely using the respective glucose uptake rates as input. For instance, we correctly predicted growth rates (Fig. 3a), a respiratory metabolism at low GURs ($< 3 \text{ mmol gCDW}^{-1} \text{ h}^{-1}$, Fig. 3b–d) and aerobic fermentation with lowered oxygen uptake rates at GURs $> 3 \text{ mmol gCDW}^{-1} \text{ h}^{-1}$ (Fig. 3b,c). At a GUR of $22 \text{ mmol gCDW}^{-1} \text{ h}^{-1}$, we predicted a maximal growth rate followed by a decrease in the growth rate and glycerol production at greater GURs, while still maximizing the growth rate in the optimization. The fact that we could not find any experimental values with GURs $> 22 \text{ mmol gCDW}^{-1} \text{ h}^{-1}$ suggests that cells restrict their glucose uptake rate to retain the maximal possible growth rate.

FBA simulations without a limit on g^{diss} predicted a respiratory metabolism for all GURs and no maximal growth rate (compare dotted lines in Fig. 3a–d). FBA simulations with other frequently used objectives ('minimal sum of absolute fluxes', 'maximal ATP yield', 'maximal ATP yield per flux sum' and 'maximal biomass per flux sum') and the $g^{\text{diss}}_{\text{lim}}$ constraint did not correctly predict the physiologies (compare dashed lines in Fig. 3a–d and Supplementary Fig. 6). Together with exhaustive sensitivity analyses of various model parameters, for example lower and upper bounds of the intracellular metabolite concentrations, and Gibbs energies of reaction (Supplementary Figs. 3–5), this shows that the predictions obtained with growth maximization as objective and the constrained cellular Gibbs energy dissipation rate are not a trivial result of the earlier regression, nor are they enforced by isolated elements of our model.

To further examine the predictions obtained with the model constrained by the rate limit on Gibbs energy dissipation, we compared intracellular flux predictions with results from ^{13}C -based metabolic flux analysis (^{13}C -MFA). We found that our predictions were in agreement with fluxes determined with ^{13}C -MFA, as was evident from metabolic reactions located at key branch points in

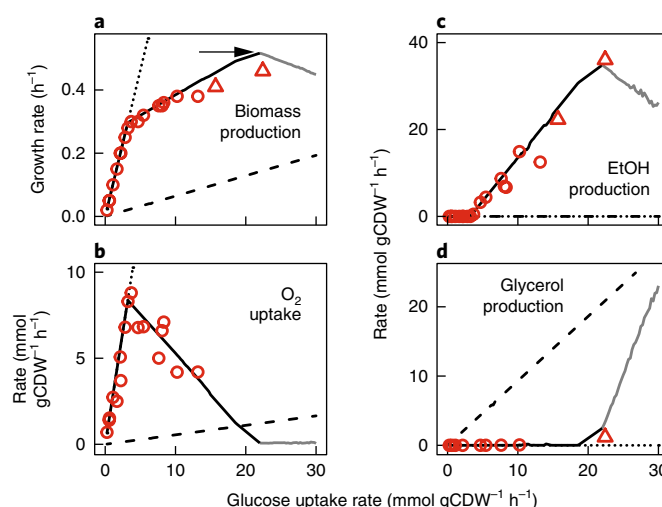


Fig. 3 | Accurate predictions of cellular physiology with flux balance analysis using the combined thermodynamic and stoichiometric model constrained by $g^{\text{diss}}_{\text{lim}}$. a–d, Predictions of physiological rates for *S. cerevisiae* growth on glucose (solid black line) with growth maximization as objective and constrained by the $g^{\text{diss}}_{\text{lim}}$ of $-3.7 \text{ kJ gCDW}^{-1} \text{ h}^{-1}$ as a constraint. Red circles represent experimentally determined values from glucose-limited chemostat cultures^{17,52} and red triangles values from glucose batch cultures^{52,53}. The black arrow points to the GUR at which the maximum growth rate was observed; solid grey lines represent predictions above this GUR. The dotted black lines represent FBA simulations with growth maximization as an objective, but without a constraint in g^{diss} . The dashed black lines represent predictions with the 'minimal sum of absolute fluxes' as an objective and the $g^{\text{diss}}_{\text{lim}}$ constraint.

central metabolism (Fig. 4a–d and Supplementary Fig. 7). We found the flux reorganization patterns we expected; for instance, redirection of flux from the pentose-phosphate pathway to glycolysis with increasing GUR (Fig. 4a,b).

The fact that we could correctly predict extracellular physiologies including the maximal growth rate, as well as the experimentally observed reorganization pattern of intracellular metabolic fluxes with increasing GURs, suggests that the objective of growth maximization under the constraint of an upper limit on the Gibbs energy dissipation rate could have governed the evolution of metabolism and its regulation, at least in yeast.

Identified principle also applies to *Escherichia coli*. Because we conjectured that the two elements of this principle, growth maximization and the upper limit on the Gibbs energy dissipation rate, might be universal, we next investigated whether this principle also applies to prokaryotes, using *E. coli* as model. By following the same workflow as we outlined for *S. cerevisiae*, we formulated a combined thermodynamic and stoichiometric metabolic model, this time at genome scale, encompassing 626 unique metabolites involved in 1,062 metabolic processes²³ (Supplementary Methods 1.1–1.5, Supplementary Note 2 and Supplementary Data 2). Using this model and non-linear regression (Supplementary Methods 3.1 and 3.2) with data from glucose-limited chemostat cultures²⁴, we found, similarly to the yeast results, that g^{diss} first linearly increased with increasing GURs and then reached a plateau (at $-4.9 \text{ kJ gCDW}^{-1} \text{ h}^{-1}$) at conditions in which acetate is excreted (Supplementary Figs. 9 and 10). When we performed FBA simulations with growth maximization as the objective and the identified $g^{\text{diss}}_{\text{lim}}$ as constraint (Supplementary Methods 3.3 and 3.4), we again correctly predicted the shift from respiration to fermentation with increasing GURs, as

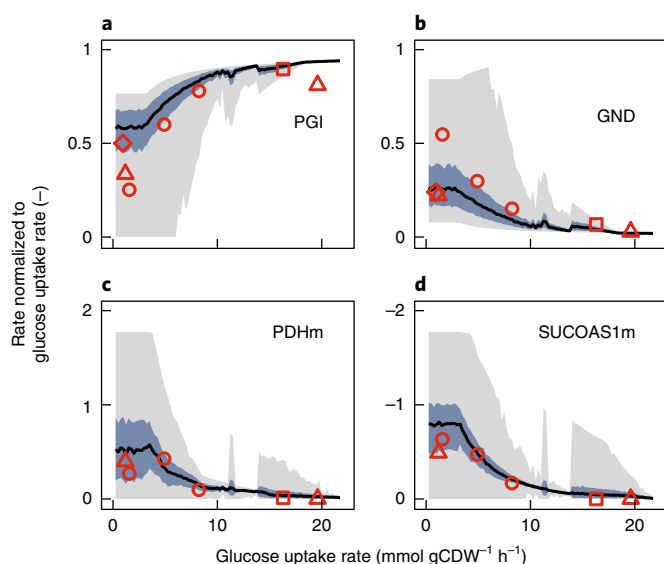


Fig. 4 | Accurate predictions of intracellular fluxes with flux balance analysis using the model constrained by $g_{\text{lim}}^{\text{diss}}$. **a–d**, Intracellular fluxes at key branch points in central metabolism predicted by FBA and inferred through ^{13}C -based metabolic flux analysis. These FBA predictions were obtained by flux variability analysis with growth rates fixed to values obtained in FBA optimizations and sampling of the solution space (Supplementary Fig. 8 and Supplementary Methods 2.3 and 2.4). The graphs show flux boundaries from flux variability analyses (light grey areas) and multivariate distribution of intracellular fluxes obtained by sampling the solution space ($n=10,000,000$) of the $g_{\text{lim}}^{\text{diss}}$ -constrained model for optimal growth rates, with black lines representing medians and dark blue areas the 97.5% confidence intervals. The symbols denote fluxes determined by ^{13}C -MFA: diamonds⁵⁴, squares⁵⁵, triangles⁵⁶ and circles⁵⁷. The models used for ^{13}C -MFA were small networks with about 20–30 reactions and included heuristic assumptions about the reversibility of metabolic reactions. Therefore, the experimental flux estimates may contain errors and biases as described⁵⁴ and should be understood as a comparison rather than a benchmark. PGI, glucose-6-phosphate isomerase; GND, phosphoglucose dehydrogenase; PDHm, pyruvate dehydrogenase; SUCOAS1m, succinate-CoA ligase. Additional intracellular fluxes are shown in Supplementary Fig. 7.

well as the maximal growth rate (Fig. 5a). Notably, this flux reorganization pattern was reflected in measured changes in protein abundance (Supplementary Fig. 11).

Next, we used this model to perform FBA simulations with different nutrients in which we allowed for unlimited substrate uptake. Specifically, we simulated growth in unlimited batch cultures on eight different carbon sources (acetate, fructose, galactose, gluconate, glucose, glycerol, pyruvate and succinate), on simultaneously present glucose and succinate and on either glucose or glycerol supplemented with all proteinogenic amino acids; notably, none of these conditions were used in the regression. Here, we found that our model could predict maximal growth rates, as well as uptake and excretion rates (Fig. 5b and Supplementary Fig. 12). Notably, this was true even for cases in which we simulated complex media with the possibility of unlimited uptake of all proteinogenic amino acids. The same model, not constrained by the upper rate limit on Gibbs energy dissipation, did not predict maximal growth rates (as maximization of growth would lead to infinite substrate uptake and thus to infinite growth), and did not predict the fermentative phenotypes (Supplementary Fig. 13). A comparison of the FBA-predicted intracellular fluxes with ^{13}C -MFA-inferred flux distributions also showed good agreement (Supplementary Fig. 14).

As our model connects fluxes and metabolite levels through Gibbs energies of reaction and the second law of thermodynamics, we next asked whether metabolic rearrangements, which are necessary with increasing GURs, would require metabolite levels to follow certain trends. Indeed, for 36 metabolites we found a correlation (Spearman correlation coefficient > 0.6) between their concentrations and GUR. Of these 36 metabolites, experimental data as a function of GUR were available for coenzyme A, ribose 5-phosphate and α -ketoglutarate. The profiles of these metabolites matched well with the predicted profiles (Fig. 5c). Notably, α -ketoglutarate is an important metabolic regulatory molecule²⁵. Our analysis suggests that the concentration of this metabolite is constrained in a GUR-dependent manner by thermodynamics, thus making it an ideal candidate as a regulatory metabolite.

The agreement of these *E. coli* predictions with respective experimental data, extending even to the predictions of some metabolite concentrations, suggests that growth maximization under the constraint of a limited cellular Gibbs energy dissipation rate as a metabolism-governing principle also applies to *E. coli* and carbon sources other than glucose, including complex media. This provides evidence that this principle universally shaped cellular metabolism across organisms. Furthermore, as the *E. coli* model used is a genome-scale model, this shows that the concept can also be implemented and applied on the genome scale.

Maximal growth under the rate limit on Gibbs energy dissipation.

Finally, we aimed to understand how $g_{\text{lim}}^{\text{diss}}$ governs metabolism. Therefore, we revisited yeast and the respective FBA simulations from which we determined the Gibbs energy dissipation rate of each metabolic process, g , at different GURs. From these process- and GUR-specific dissipation rates, we identified seven clusters of metabolic processes that showed similar Gibbs energy dissipation trends with increasing GURs (Fig. 6a and Supplementary Fig. 15). We found that, below GURs of $3 \text{ mmol gCDW}^{-1} \text{ h}^{-1}$, processes related to respiration (respiration and energy metabolism clusters in Fig. 6a) contributed 45% to the total cellular Gibbs energy dissipation rate, which, in absolute terms, is still low at this point. Once $g_{\text{lim}}^{\text{diss}}$ was reached and GUR further increased, cells redirected metabolic fluxes from dissipation-intense pathways to less dissipation-intense pathways, that is, to fermentative processes (pyruvate decarboxylase and pyruvate kinase clusters in Fig. 6a), which produced $\sim 40\%$ of the $g_{\text{lim}}^{\text{diss}}$ at GURs $> 20 \text{ mmol gCDW}^{-1} \text{ h}^{-1}$.

Such flux redirection occurred not only between respiration and fermentation, but also between other processes as indicated by the changes in the directionality patterns (Supplementary Fig. 17). Thus, the flux redirection, which occurs at increasing GURs, allows cells to achieve higher growth rates while staying below $g_{\text{lim}}^{\text{diss}}$. Such flux redirection leads to the usage of pathways with lower carbon efficiencies and thus lower biomass yields (Fig. 6b). Once all possibilities for flux redirection are exhausted, upon a further enforced increase in the nutrient uptake, cells need to reduce their growth rate and to excrete other by-products (for instance, glycerol) to stay below the Gibbs energy dissipation rate limit. This defines the maximal growth rate (compare Fig. 2).

Discussion

Our findings answer central questions in metabolic research, for example what shapes metabolic fluxes, what limits growth rate, and what causes cells to change the way they operate their metabolism, as exemplified by the paradigm switch from respiration to aerobic fermentation. Although we cannot exclude the possibility of a third correlated factor explaining our results, our work proposes growth maximization under the constraint of an upper limit on the cellular Gibbs energy dissipation rate as the basic principle underlying metabolism; this also offers an explanation for the empirical description of Pareto optimality in metabolism²⁶

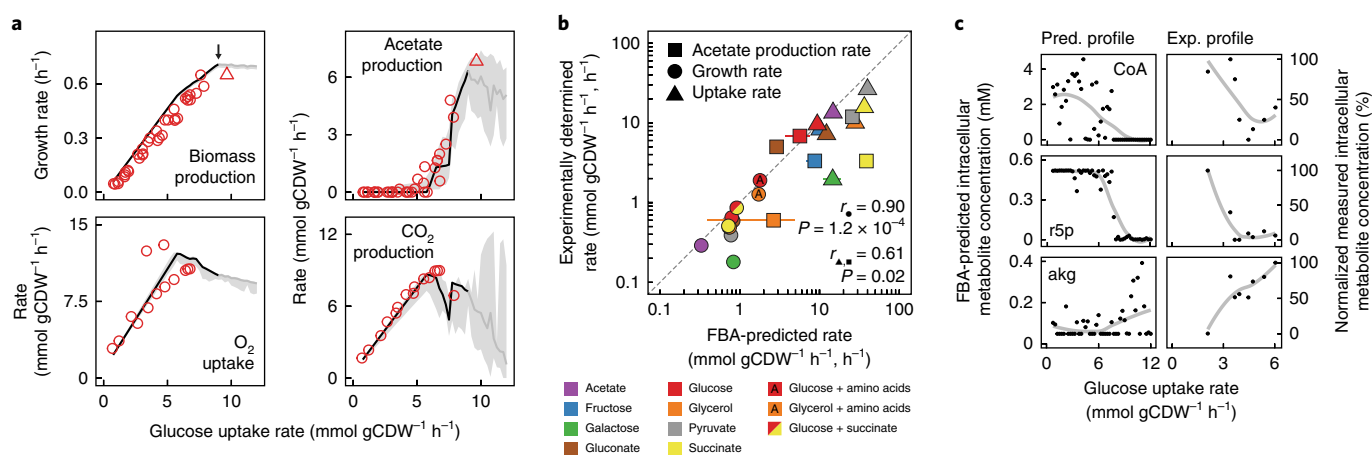


Fig. 5 | Predictive capabilities of flux balance analysis using the genome-scale combined thermodynamic and stoichiometric model of *E. coli* constrained by $g^{\text{diss}}_{\text{lim}}$. **a**, Predictions of physiological rates for *E. coli* growth on glucose with growth maximization as objective and the $g^{\text{diss}}_{\text{lim}}$ of $-4.9 \text{ kJ gCDW}^{-1} \text{ h}^{-1}$ as a constraint (solid black line). Red circles represent experimentally determined values from glucose-limited chemostat cultures^{24,58–61}, and red triangles represent values from glucose batch cultures⁶². The black arrow points to the GUR, at which the maximum growth rate was obtained in the simulation; solid grey lines represent predictions above this GUR and shaded grey area the variability determined through variability analysis. **b**, Predictions of maximal growth phenotype for growth on eight different carbon sources, on simultaneously present glucose and succinate, or on either glucose or glycerol supplemented with all proteinogenic amino acids, in all cases allowing for unlimited carbon source uptake^{63,64}. Horizontal error bars represent variability determined at optimal solution. The goodness of FBA predictions was assessed using the Pearson correlation coefficient (r), where the P values were derived using Student's t -test. **c**, Concentration profiles of three metabolites (coenzyme A, CoA; ribose-5-phosphate, r5p; and α -ketoglutarate, akg), which in our simulations were correlated with GUR, and for which experimental data were available. The experimental metabolite profiles were obtained in accelerostat experiments with the *E. coli* strain MG1655 (ref. 59). Here the onset of acetate production occurred at a lower GUR of $3.6 \text{ mmol gCDW}^{-1} \text{ h}^{-1}$. For both predictions and experimental data, the concentration profiles (solid grey line) were obtained using a local polynomial regression method.

(Supplementary Fig. 18). The limit on cellular Gibbs energy dissipation rate leads to a redirection of metabolic fluxes (for instance, from respiration to fermentation) as substrate uptake rates increase and cells try to maximize growth.

Although the second law of thermodynamics was traditionally formulated for isolated systems close to equilibrium¹², here we applied it to cells—open systems out of equilibrium—similarly to how the law has been applied to cellular metabolism^{13,19,27–32}. Following Erwin Schrödinger's notion that “the essential thing in metabolism is that the organism succeeds in freeing itself from all the entropy it cannot help producing while alive”³³, our work suggests that there is an upper rate limit at which cells can do so.

The identified upper rate limit on cellular Gibbs energy dissipation suggests that higher rates of Gibbs energy dissipation cannot be sustained, because this presumably has detrimental consequences for the functioning of cells. What could such consequences be? If the dissipated Gibbs energy is dissipated as heat, then the identified limit could be understood as a limit on heat transfer. Although it was suggested that mitochondria (a compartment in which, at certain conditions, we predicted >50% of the total cellular Gibbs energy dissipation; compare Fig. 6) could have an elevated temperature^{34,35}, theoretical considerations argue against a significant and detrimental temperature increase inside individual cells³⁶. On the other hand, during enzymes' catalytic cycle, enzymes might be set in motion, and Gibbs energy is therefore translated into work^{37–40}. In fact, active metabolism was shown to increase cytoplasmic diffusion rates above those expected from thermal motion alone^{41–43}. In turn, cytoplasmic motion can negatively affect biomolecular functions, such as kinetic proofreading and gene regulation^{44,45}. Therefore, the upper limit on the rate of cellular Gibbs energy dissipation could reflect the limit of critical non-thermal motion inside the cell, beyond which biomolecular function would be compromised.

To maximize growth rate and at the same time avoid exceeding the critical Gibbs energy dissipation rate, cells must have evolved respective sensing mechanisms and means to control metabolic

fluxes by adjusting enzyme abundance and kinetics. If intracellular molecule motion reflects the cellular Gibbs energy dissipation rate, then this could directly lead to differential regulation of gene expression. Alternatively, the recently uncovered cellular capability for metabolic flux sensing and flux-dependent regulation^{11,46} could have evolved in a manner to ultimately avoid detrimental Gibbs energy dissipation rates.

Our approach of using a limit in the cellular Gibbs energy dissipation rate is structurally similar to recent approaches using protein allocation constraints^{8,9}, with a weighted sum of fluxes being the limiting element in both. In the protein allocation approaches, metabolic fluxes are weighted, for example by the molecular mass and the catalytic efficiency of the respective enzymes⁹. In contrast to these static weights, weighting in our approach is provided by the Gibbs energies of reaction, which can vary to some extent, being a function of flexible metabolite concentrations. We argue that the similarity not only is technical, but also probably has a biological or physical reason: to harness the energy released during catabolism, cells need to partition their metabolism into reaction steps that release Gibbs energy amounts that can be stored, for example as ATP. Thus an overall larger change in Gibbs energy in a pathway (for example, as in respiration compared to fermentation) requires more reaction steps, and thus a larger amount of enzyme.

Our work shows that cellular metabolism could be constrained by a limit on the cellular Gibbs energy dissipation rate. This limit is likely a universal, physical constraint on metabolism and could also explain the Warburg effect in cancer cells. Future work will need to show how the Gibbs energy dissipation rate limits biomolecular function, and how it could have shaped the evolution of enzyme expression and kinetics. Moreover, our concept for metabolic flux prediction, although computationally demanding, offers an advantage over current FBA-based methods as it does not require assumptions about reaction directionalities and does not require any organism-specific information that is hard to obtain, such as information on protein abundances and catalytic efficiencies⁴⁷.

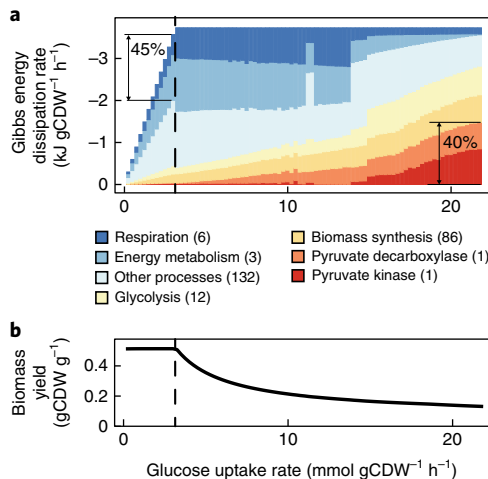


Fig. 6 | Cells redistribute flux to avoid critical Gibbs energy dissipation rates. a, The limit on the Gibbs energy dissipation rate causes flux redistribution with increasing GURs, globally leading to a change from respiratory to fermentative pathways. Seven clusters of metabolic processes were identified by cluster analysis using the Euclidean distance between the Gibbs energy dissipation rates of metabolic processes at different GURs (details of the processes in the clusters are in Supplementary Fig. 15). The Gibbs energy dissipation rates of the metabolic processes were obtained by sampling the solution space of the $g^{\text{diss}}_{\text{lim}}$ -constrained model for optimal growth. The numbers in brackets indicate number of processes in each cluster. The dashed line indicates the GUR at which ethanol production starts. An identical analysis of the data from the regression yielded similar results (compare Supplementary Fig. 16). Out of the 31 possible ATP- or NAD(P)H-consuming futile cycles, none carried a flux in the FBA optimizations and thus Gibbs energy is not dissipated through futile cycles. **b**, The shift to less carbon-efficient pathways leads to reduced biomass yields with increasing GURs.

Thus, with this work, we not only present a fundamental understanding of metabolism, but also provide an important contribution to predictive metabolic modelling.

Methods

Formulation of the combined thermodynamic and stoichiometric model. The combined thermodynamic and stoichiometric network model is based on steady-state mass balances for the metabolites i :

$$\sum_{j \in \text{MET}} S_{ij} v_j = v_{i \in \text{EXG}} \quad \forall i \quad (1)$$

where S_{ij} are the stoichiometric coefficients of the metabolic ($j \in \text{MET}$) and exchange ($i \in \text{EXG}$) processes; $v_{j \in \text{MET}}$ are the rates of metabolic processes, that is, chemical conversions and/or metabolite transport; and $v_{i \in \text{EXG}}$ are the rates of exchange processes, which describe the transfer of metabolites across the system boundary. In this stoichiometric network model, we included steady-state, pH-dependent proton and charge balances for each intracellular compartment; this imposes metabolic fluxes that keep the pH in the respective compartments and the membrane potentials across the membranes constant (Supplementary Methods 1.1).

In addition to the mass, proton and charge balances, we introduced a Gibbs energy balance, which states that g^{diss} equals the sum of Gibbs energy exchange rates, $g_{i \in \text{EXG}}$ and the sum of Gibbs energy dissipation rates, $g_{j \in \text{MET}}$:

$$g^{\text{diss}} = \sum_{i \in \text{EXG}} g_i = \sum_{j \in \text{MET}} g_j \quad (2)$$

The Gibbs energy exchange rates are defined as:

$$g_i = \Delta_f G'_i v_i \quad \forall i \in \text{EXG} \quad (3)$$

where $\Delta_f G'_{i \in \text{EXG}}$ are the Gibbs energies of formation of the metabolites transferred across the system boundary. The Gibbs energy dissipation rates are defined as:

$$g_j = \Delta_r G'_j v_j \quad \forall j \in \text{MET} \quad (4)$$

where $\Delta_r G'_{j \in \text{MET}}$ are the Gibbs energies of reaction of the cellular metabolic processes.

The Gibbs energies of reaction of the metabolic processes, $\Delta_r G'_{j \in \text{MET}}$, are due to chemical conversions and/or metabolite transport according to:

$$\Delta_r G'_j = \Delta_r G'^0_j + \Delta_r G'^t_j + RT \sum_{i \notin h^+} S_{ij} \ln c_i \quad \forall j \in \text{MET} \quad (5)$$

where $\Delta_r G'^0_{j \in \text{MET}}$ are the standard Gibbs energies of the chemical conversions, $\Delta_r G'^t_{j \in \text{MET}}$ the Gibbs energies of the metabolite transports, $\ln c_i$ the natural logarithm of the concentration c_i of the metabolite i , T the temperature and R the universal gas constant.

To define the Gibbs energy exchange rates, we used Gibbs energies of formations, $\Delta_f G'_{i \in \text{EXG}}$, of the respective metabolites $i \in \text{EXG}$ that are transferred across the system boundary:

$$\Delta_f G'_i = \Delta_f G'^0_i + RT \ln c_i \quad \forall i \in \text{EXG} \quad (6)$$

where $\Delta_f G'^0_{i \in \text{EXG}}$ are the standard Gibbs energies of formation of the metabolites $i \in \text{EXG}$.

All standard Gibbs energies were estimated using the component-contribution method¹⁸ and transformed¹⁶ (indicated by the prime symbol) to the pH values in the respective compartment. Furthermore, we used the extended Debye-Hückel equation to take into account the effect of electrolyte solution on charged metabolites¹⁶ (Supplementary Methods 1.2 and 1.3).

The directionalities of the fluxes through the metabolic processes $j \in \text{MET}$ were in principle assumed to be reversible but must obey the second law of thermodynamics, according to:

$$g_j < 0 \quad (j \in \text{MET} \wedge v_j \neq 0) \quad (7)$$

where the Gibbs energy dissipation rate, $g_{j \in \text{MET}}$, must be < 0 , in case there is flux through this metabolic process (Supplementary Methods 1.4).

By combining the relevant equations mentioned above, we formulated the combined thermodynamic and stoichiometric model, $M(v, \ln c) \leq 0$, as a set of equalities and inequalities of the variables v , that is, the rates of the metabolic processes $j \in \text{MET}$ and the exchange processes $i \in \text{EXG}$ and $\ln c$, the natural logarithm of the concentrations of the metabolites i :

$$\{M(v, \ln c) \leq 0\} \hat{=} \left\{ \begin{array}{l} \sum_{j \in \text{MET}} S_{ij} v_j = v_{i \in \text{EXG}} \quad \forall i \\ g^{\text{diss}} = \sum_{i \in \text{EXG}} g_i \\ g^{\text{diss}} = \sum_{j \in \text{MET}} g_j \\ g_j = \Delta_r G'_j v_j \quad \forall j \in \text{MET} \\ g_i = \Delta_f G'_i v_i \quad \forall i \in \text{EXG} \\ \Delta_r G'_j = \Delta_r G'^0_j + \Delta_r G'^t_j + RT \sum_{i \notin h^+} S_{ij} \ln c_i \quad \forall j \in \text{MET} \\ \Delta_f G'_i = \Delta_f G'^0_i + RT \ln c_i \quad \forall i \in \text{EXG} \\ g_j < 0 \quad \forall (j \in \text{MET} \wedge v_j \neq 0) \end{array} \right. \quad (8)$$

Before performing mathematical optimizations with this non-linear and non-convex model, we applied two strategies to reduce the size of the model without reducing its degrees of freedom. First, we defined the scope of the predictions in terms of allowed exchange processes and removed all reactions from the model that could never carry metabolic flux under the specified conditions. Second, we identified reactions, which are fully coupled (that is, always proportionally carry the same flux) as described⁴⁸, and reformulated the model, $M(v, \ln c) \leq 0$, by replacing the reaction fluxes v with the flux through the group of coupled reactions, v^{grp} . Note that the reduced model, $M^{\text{grp}}(v, \ln c) \leq 0$, still strictly only depends on the fluxes v and metabolite concentrations $\ln c$, and that whereas the mass balances and Gibbs energy balance are formulated using the flux through the reaction groups v^{grp} , the second law of thermodynamics is still formulated for every metabolic process individually so as not to lose any directionality constraints.

The reduced model together with a set of bounds, $B(v, \ln c) \leq 0$, on the variables v and $\ln c$, define the solution space Ω . Ω contains the mass-, proton- and charge-balanced and thermodynamically feasible steady-state solutions, in terms of rates v and metabolite concentrations $\ln c$. The set of bounds, $B(v, \ln c) \leq 0$, consist of constraints on the rates of the extracellular exchange processes, for example the uptake rate of a carbon source, the physiological ranges of the intracellular metabolite concentrations, $\ln c$, and Gibbs energies of reactions, $\Delta_r G'$, or an upper limit on g^{diss} . We analyzed the solution space, Ω , using mathematical optimization, where we formulated different optimization problems, for example regression, flux balance and variability analyses (Supplementary Methods 1.5).

Implementation. Because Ω is non-convex and non-linear, the optimization problems can contain multiple local optima. To efficiently solve these problems, we first determined an approximate solution by solving a linear relaxation of the optimization problem with the mixed-integer programming solver CPLEX 12 (IBM ILOG). Then, we used this approximate solution as starting point for the solution of the optimization problem with the global optimization solver ANTIGONE 1.0 (ref. ²¹) or the local solver CONOPT3 (ref. ⁴⁹).

Generally, we implemented all optimization problems in the mathematical programming system General Algebraic Modeling System (GAMS) (GAMS Development Corporation, release 24.2.2). The optimization problems were solved on computational clusters; we used a small test cluster of 30 cores for model development. For the large-scale studies in which we solved >100,000 optimization problems, we set up a cluster in Amazon's Elastic Compute Cloud comprising 1,248 cores, or used a managed HPC cluster comprising 5,640 cores. Solving these optimization problems typically took between 30 min and 14 h (Supplementary Methods 1.6).

Regression analysis. We estimated the g^{dis} values and a thermodynamically consistent set of standard Gibbs energies of reactions, $\Delta_r G'^{\circ}$, from experimental data and the reduced model, $M^{\text{RP}}(v, \ln c) \leq 0$. The experimental data consisted of (1) measured extracellular physiological rates and (2) intracellular metabolite concentrations (only for *S. cerevisiae*), which were both determined for glucose-limited chemostat cultures at different dilution rates, and (3) standard Gibbs energies of reactions, determined from the component contribution method¹⁸.

We formulated a non-linear regression analysis that we regularized using the Lasso method⁵⁰. This regularization, which was done to prevent overfitting the data, included a regularization parameter α , which was determined by model selection. The regression comprised two steps: (1) determining the minimal training error as a function of α and (2) determining the goodness of fit using the reduced chi-squared $\chi^2_{\text{red},\alpha}$ as a function of α . The model selection was performed by repeating these two steps for different α values and selecting the α with a reduced $\chi^2_{\text{red},\alpha}$ of 1, which means that the model and the data fit each other (Supplementary Methods 2.1 and 3.1).

Next, we determined physiological bounds for the Gibbs energies, $\Delta_r G'_{j \in \text{MET}}$, of the metabolic processes $j \in \text{MET}$ and for the metabolite concentrations c_i . These physiological bounds (lower, lo ; upper, up) are required in our strategy to solve the FBA optimizations to formulate the linear relaxation and were defined by the infimum and supremum, that is, the smallest and greatest possible values of c and $\Delta_r G'$ across all experimental conditions of the data sets as determined by variability analysis (Supplementary Methods 2.2 and 3.2).

Flux balance analysis with the combined thermodynamic and stoichiometric model. For different growth conditions, that is, glucose uptake rates or carbon sources, we predicted metabolic fluxes using the reduced model, $M^{\text{RP}}(v, \ln c) \leq 0$, and FBA. Therefore, we defined the solution spaces of the FBA, Ω^{FBA} . The metabolite concentrations, $\ln c$, and the Gibbs energies of reaction, $\Delta_r G'$, were constrained by the regression-identified physiological bounds, and the standard Gibbs energies of reactions, $\Delta_r G'^{\circ}$, were set to the identified thermodynamically consistent set. Furthermore, g^{dis} was constrained by $g^{\text{dis}}_{\text{lim}}$ and the rates of exchange processes were constrained by the growth condition, such that any quantity of oxygen, phosphate, ammonium, water, protons, sulfate, and so on (resembling what was available in the growth medium) could be taken up, and all other compounds could be excreted.

Then, we used FBA¹⁴, in which we maximized the growth rate, μ , in the solution space Ω^{FBA} ,

$$\mu^* = \max\{v_{\text{BMSYN}} : (v, \ln c) \in \Omega^{\text{FBA}}\} \quad (9)$$

where μ^* is the optimal growth rate at a specific condition, and BMSYN is the biomass synthesis reaction (Supplementary Methods 2.3 and 3.3).

We then characterized the solution space $\Omega^{\text{FBA}}_{\mu^*}$ for optimal growth rates, using flux variability analysis, and, as described^{14,26,51}, using Markov-chain Monte Carlo (MCMC) sampling (Supplementary Methods 2.4 and 3.4).

Reporting Summary. Further information on research design is available in the Nature Research Reporting Summary linked to this article.

Data availability

The data that support the plots within this paper and other findings of this study are available from the corresponding author upon reasonable request. The code is available from the corresponding author upon request and the code to perform the flux balance analyses is deposited on GitHub (<https://doi.org/10.5281/zenodo.1401220>).

Received: 11 May 2018; Accepted: 23 October 2018;
Published online: 7 January 2019

References

- Molenaar, D., Van Berlo, R., De Ridder, D. & Teusink, B. Shifts in growth strategies reflect tradeoffs in cellular economics. *Mol. Syst. Biol.* **5**, 323 (2009).
- Basan, M. et al. Overflow metabolism in *Escherichia coli* results from efficient proteome allocation. *Nature* **528**, 99–104 (2015).
- Rozpędowska, E. et al. Parallel evolution of the make–accumulate–consume strategy in *Saccharomyces* and *Dekkera* yeasts. *Nat. Commun.* **2**, 302 (2011).
- Beg, Q. K. et al. Intracellular crowding defines the mode and sequence of substrate uptake by *Escherichia coli* and constrains its metabolic activity. *Proc. Natl Acad. Sci. USA* **104**, 12663–12668 (2007).
- Zhuang, K., Vemuri, G. N. & Mahadevan, R. Economics of membrane occupancy and respiro-fermentation. *Mol. Syst. Biol.* **7**, 500–500 (2014).
- Koppenol, W. H., Bounds, P. L. & Dang, C. V. Otto Warburg's contributions to current concepts of cancer metabolism. *Nat. Rev. Cancer* **11**, 325–337 (2011).
- Vander Heiden, M. G., Cantley, L. C. & Thompson, C. B. Understanding the Warburg effect: the metabolic requirements of cell proliferation. *Science* **324**, 1029–1033 (2009).
- Mori, M., Hwa, T., Martin, O. C., De Martino, A. & Marinari, E. Constrained allocation flux balance analysis. *PLoS Comput. Biol.* **12**, e1004913 (2016).
- Sánchez, B. J. et al. Improving the phenotype predictions of a yeast genome-scale metabolic model by incorporating enzymatic constraints. *Mol. Syst. Biol.* **13**, 935 (2017).
- Zabalza, A. et al. Regulation of respiration and fermentation to control the plant internal oxygen concentration. *Plant Physiol.* **149**, 1087–1098 (2009).
- Huberts, D. H. E. W., Niebel, B. & Heinemann, M. A flux-sensing mechanism could regulate the switch between respiration and fermentation. *FEMS Yeast. Res.* **12**, 118–128 (2012).
- von Bertalanffy, L. The theory of open systems in physics and biology. *Science* **111**, 23–29 (1950).
- von Stockar, U. Biothermodynamics of live cells: a tool for biotechnology and biochemical engineering. *J. Non-equilib. Thermodyn.* **35**, 415–475 (2010).
- Lewis, N. E., Nagarajan, H. & Palsson, B. O. Constraining the metabolic genotype–phenotype relationship using a phylogeny of in silico methods. *Nat. Rev. Microbiol.* **10**, 291–305 (2012).
- Jol, S. J., Kümmel, A., Hatzimanikatis, V., Beard, D. A. & Heinemann, M. Thermodynamic calculations for biochemical transport and reaction processes in metabolic networks. *Biophys. J.* **99**, 3139–3144 (2010).
- Alberty, R. A. et al. Recommendations for terminology and databases for biochemical thermodynamics. *Biophys. Chem.* **155**, 89–103 (2011).
- Canelas, A. B., Ras, C., ten Pierick, A., van Gulik, W. M. & Heijnen, J. J. An in vivo data-driven framework for classification and quantification of enzyme kinetics and determination of apparent thermodynamic data. *Metab. Eng.* **13**, 294–306 (2011).
- Noor, E., Haraldsdóttir, H. S., Milo, R. & Fleming, R. M. T. Consistent estimation of Gibbs energy using component contributions. *PLoS Comput. Biol.* **9**, e1003098 (2013).
- Beard, D., Liang, S. & Qian, H. Energy balance for analysis of complex metabolic networks. *Biophys. J.* **83**, 79–86 (2002).
- Price, N. D., Famili, I., Beard, D. A. & Palsson, B. O. Extreme pathways and Kirchhoff's second law. *Biophys. J.* **83**, 2879–2882 (2002).
- Misener, R. & Floudas, C. A. ANTIGONE: Algorithms for coNTinuous / Integer Global Optimization of Nonlinear Equations. *J. Glob. Optim.* **59**, 503–526 (2014).
- Schuetz, R., Kuepfer, L. & Sauer, U. Systematic evaluation of objective functions for predicting intracellular fluxes in *Escherichia coli*. *Mol. Syst. Biol.* **3**, 119 (2007).
- Reed, J. L., Vo, T. D., Schilling, C. H. & Palsson, B. O. An expanded genome-scale model of *Escherichia coli* K-12 (iJR904 GSM/GPR). *Genome. Biol.* **4**, R54 (2003).
- Vemuri, G. N., Altman, E., Sangurdekar, D. P., Khodursky, A. B. & Eiteman, M. A. Overflow metabolism in *Escherichia coli* during steady-state growth: transcriptional regulation and effect of the redox ratio. *Appl. Environ. Microbiol.* **72**, 3653–3661 (2006).
- You, C. et al. Coordination of bacterial proteome with metabolism by cyclic AMP signalling. *Nature* **500**, 301–306 (2013).
- Schuetz, R., Zamboni, N., Zampieri, M., Heinemann, M. & Sauer, U. Multidimensional Optimality of Microbial Metabolism. *Science* **336**, 601–604 (2012).
- Kümmel, A., Panke, S. & Heinemann, M. Putative regulatory sites unraveled by network-embedded thermodynamic analysis of metabolome data. *Mol. Syst. Biol.* **2**, 2006.0034 (2006).
- Henry, C. S., Broadbelt, L. J. & Hatzimanikatis, V. Thermodynamics-based metabolic flux analysis. *Biophys. J.* **92**, 1792–1805 (2007).
- Fleming, R. M. T., Thiele, I. & Nashueuer, H. P. Quantitative assignment of reaction directionality in constraint-based models of metabolism: application to *Escherichia coli*. *Biophys. Chem.* **145**, 47–56 (2009).
- Bennett, B. D. et al. Absolute metabolite concentrations and implied enzyme active site occupancy in *Escherichia coli*. *Nat. Chem. Biol.* **5**, 593–599 (2009).

31. Bordel, S. & Nielsen, J. Identification of flux control in metabolic networks using non-equilibrium thermodynamics. *Metab. Eng.* **12**, 369–377 (2010).
32. Noor, E. et al. Pathway thermodynamics highlights kinetic obstacles in central metabolism. *PLoS Comput. Biol.* **10**, e1003483 (2014).
33. Schrödinger, E. *What Is Life? The Physical Aspect of the Living Cell* (Cambridge Univ. Press, 1944).
34. Okabe, K. et al. Intracellular temperature mapping with a fluorescent polymeric thermometer and fluorescence lifetime imaging microscopy. *Nat. Commun.* **3**, 705 (2012).
35. Lane, N. Hot mitochondria? *PLoS Biol.* **16**, e2005113 (2018).
36. Baffou, G., Rigneault, H., Marguet, D. & Jullien, L. A critique of methods for temperature imaging in single cells. *Nat. Methods* **11**, 899–901 (2014).
37. Weber, J. K., Shukla, D. & Pande, V. S. Heat dissipation guides activation in signaling proteins. *Proc. Natl. Acad. Sci. USA* **112**, 10377–10382 (2015).
38. Slochow, D. R. & Gilson, M. K. Motor-like properties of nonmotor enzymes. *Biophys. J.* **114**, 2174–2179 (2018).
39. Riedel, C. et al. The heat released during catalytic turnover enhances the diffusion of an enzyme. *Nature* **517**, 227–230 (2014).
40. Golestanian, R. Anomalous diffusion of symmetric and asymmetric active colloids. *Phys. Rev. Lett.* **102**, 188305 (2009).
41. Gallet, F., Arcizet, D., Bohec, P. & Richert, A. Power spectrum of out-of-equilibrium forces in living cells: amplitude and frequency dependence. *Soft Matter* **5**, 2947 (2009).
42. Milstein, J. N., Chu, M., Raghunathan, K. & Meiners, J. C. Two-color DNA nanoprobe of intracellular dynamics. *Nano. Lett.* **12**, 2515–2519 (2012).
43. Weber, S. C., Spakowitz, A. J. & Theriot, J. A. Nonthermal ATP-dependent fluctuations contribute to the in vivo motion of chromosomal loci. *Proc. Natl. Acad. Sci. USA* **109**, 7338–7343 (2012).
44. Chen, Y.-F., Milstein, J. N. & Meiners, J.-C. Protein-mediated DNA loop formation and breakdown in a fluctuating environment. *Phys. Rev. Lett.* **104**, 258103 (2010).
45. Milstein, J. N. & Meiners, J.-C. On the role of DNA biomechanics in the regulation of gene expression. *J. R. Soc. Interface* **8**, 1673–1681 (2011).
46. Kochanowski, K. et al. Functioning of a metabolic flux sensor in *Escherichia coli*. *Proc. Natl. Acad. Sci. USA* **110**, 1130–1135 (2013).
47. Nilsson, A., Nielsen, J. & Palsson, B. O. Metabolic models of protein allocation call for the kinome. *Cell Syst.* **5**, 538–541 (2017).
48. Burgard, A. P., Nikolaev, E. V., Schilling, C. H. & Maranas, C. D. Flux coupling analysis of genome-scale metabolic network reconstructions. *Genome Res.* **14**, 301–312 (2004).
49. Drud, A. S. CONOPT—A large-scale GRG code. *ORSA J. Comput.* **6**, 207–216 (1994).
50. Hastie, T. J., Tibshirani, R. & Friedman, J. *The Elements of Statistical Learning: Data Mining, Inference, and Prediction* (Springer-Verlag New York, 2011).
51. Schellenberger, J., Lewis, N. E. & Palsson, B. O. Elimination of thermodynamically infeasible loops in steady-state metabolic models. *Biophys. J.* **100**, 544–553 (2011).
52. van Hoek, P. et al. Effects of pyruvate decarboxylase overproduction on flux distribution at the pyruvate branch point in *Saccharomyces cerevisiae*. *Appl. Environ. Microbiol.* **64**, 2133–2140 (1998).
53. Kümmel, A. et al. Differential glucose repression in common yeast strains in response to HXK2 deletion. *FEMS Yeast. Res.* **10**, 322–332 (2010).
54. van Winden, W. et al. Metabolic-flux analysis of CEN.PK113-7D based on mass isotopomer measurements of C-labeled primary metabolites. *FEMS Yeast. Res.* **5**, 559–568 (2005).
55. Fendt, S.-M. & Sauer, U. Transcriptional regulation of respiration in yeast metabolizing differently repressive carbon substrates. *BMC Syst. Biol.* **4**, 12 (2010).
56. Gombert, A. K., Moreira dos Santos, M., Christensen, B. & Nielsen, J. Network identification and flux quantification in the central metabolism of *Saccharomyces cerevisiae* under different conditions of glucose repression. *J. Bacteriol.* **183**, 1441–1451 (2001).
57. Frick, O. & Wittmann, C. Characterization of the metabolic shift between oxidative and fermentative growth in *Saccharomyces cerevisiae* by comparative ¹³C flux analysis. *Microb. Cell. Fact.* **4**, 30 (2005).
58. Perrenoud, A. & Sauer, U. Impact of global transcriptional regulation by ArcA, ArcB, Cra, Crp, Cya, Fnr, and Mlc on glucose catabolism in *Escherichia coli*. *J. Bacteriol.* **187**, 3171–3179 (2005).
59. Valgepea, K. et al. Systems biology approach reveals that overflow metabolism of acetate in *Escherichia coli* is triggered by carbon catabolite repression of acetyl-CoA synthetase. *BMC Syst. Biol.* **4**, 166 (2010).
60. Nanchen, A., Schicker, A. & Sauer, U. Nonlinear dependency of intracellular fluxes on growth rate in miniaturized continuous cultures of *Escherichia coli*. *Appl. Environ. Microbiol.* **72**, 1164–1172 (2006).
61. Peebo, K. et al. Proteome reallocation in *Escherichia coli* with increasing specific growth rate. *Mol. Biosyst.* **11**, 1184–1193 (2015).
62. Gerosa, L. et al. Pseudo-transition analysis identifies the key regulators of dynamic metabolic adaptations from steady-state data. *Cell Syst.* **1**, 270–282 (2015).
63. Schmidt, A. et al. The quantitative and condition-dependent *Escherichia coli* proteome. *Nat. Biotechnol.* **34**, 104–110 (2015).
64. Scott, M. et al. Emergence of robust growth laws from optimal regulation of ribosome synthesis. *Mol. Syst. Biol.* **10**, 747 (2014).

Acknowledgements

This work was funded by the Netherlands Organisation for Scientific Research (NWO) through the Systems Biology Centre for Metabolism and Ageing (Groningen), and by the BE-Basic R&D Program, which was granted as FES subsidy from the Dutch Ministry of Economic Affairs, Agriculture and Innovation (EL&I). We thank A. Canelas for sharing raw data, E. Noor for help with the component contribution method, E. Wit for statistics advice, G. Zampar for helpful discussions and B. Bakker, A. Bardow, D. Huberts, A. Ortega, U. Sauer, S. Stratmann and J. Radzikowski for helpful comments on the manuscript.

Author contributions

B.N., S.L. and M.H. designed the study. B.N. and M.H. developed the concept. B.N. developed and implemented the model for *S. cerevisiae*. S.L. developed and implemented the model for *E. coli*. B.N. and S.L. carried out the simulations, analysed the data, and made the figures. B.N., S.L. and M.H. wrote the manuscript.

Competing interests

The authors declare no competing interests.

Additional information

Supplementary information is available for this paper at <https://doi.org/10.1038/s42255-018-0006-7>.

Reprints and permissions information is available at www.nature.com/reprints.

Correspondence and requests for materials should be addressed to M.H.

Publisher's note: Springer Nature remains neutral with regard to jurisdictional claims in published maps and institutional affiliations.

© The Author(s), under exclusive licence to Springer Nature Limited 2019

Reporting Summary

Nature Research wishes to improve the reproducibility of the work that we publish. This form provides structure for consistency and transparency in reporting. For further information on Nature Research policies, see [Authors & Referees](#) and the [Editorial Policy Checklist](#).

Statistical parameters

When statistical analyses are reported, confirm that the following items are present in the relevant location (e.g. figure legend, table legend, main text, or Methods section).

n/a Confirmed

- ☐ ☒ The exact sample size (*n*) for each experimental group/condition, given as a discrete number and unit of measurement
- ☐ ☒ An indication of whether measurements were taken from distinct samples or whether the same sample was measured repeatedly
- ☐ ☒ The statistical test(s) used AND whether they are one- or two-sided
Only common tests should be described solely by name; describe more complex techniques in the Methods section.
- ☒ ☐ A description of all covariates tested
- ☒ ☐ A description of any assumptions or corrections, such as tests of normality and adjustment for multiple comparisons
- ☐ ☒ A full description of the statistics including central tendency (e.g. means) or other basic estimates (e.g. regression coefficient) AND variation (e.g. standard deviation) or associated estimates of uncertainty (e.g. confidence intervals)
- ☐ ☒ For null hypothesis testing, the test statistic (e.g. *F*, *t*, *r*) with confidence intervals, effect sizes, degrees of freedom and *P* value noted
Give P values as exact values whenever suitable.
- ☒ ☐ For Bayesian analysis, information on the choice of priors and Markov chain Monte Carlo settings
- ☒ ☐ For hierarchical and complex designs, identification of the appropriate level for tests and full reporting of outcomes
- ☐ ☒ Estimates of effect sizes (e.g. Cohen's *d*, Pearson's *r*), indicating how they were calculated
- ☐ ☒ Clearly defined error bars
State explicitly what error bars represent (e.g. SD, SE, CI)

Our web collection on [statistics for biologists](#) may be useful.

Software and code

Policy information about [availability of computer code](#)

Data collection

The custom code can be obtained from authors. commercial software: Marvin14.12.1.0, ANTIGONE 1.0, CONOPT3, GAMS 24.2.2.

Data analysis

The custom code can be obtained from authors. commercial software: GAMS 24.2.2., R 3.2.0

For manuscripts utilizing custom algorithms or software that are central to the research but not yet described in published literature, software must be made available to editors/reviewers upon request. We strongly encourage code deposition in a community repository (e.g. GitHub). See the Nature Research [guidelines for submitting code & software](#) for further information.

Data

Policy information about [availability of data](#)

All manuscripts must include a [data availability statement](#). This statement should provide the following information, where applicable:

- Accession codes, unique identifiers, or web links for publicly available datasets
- A list of figures that have associated raw data
- A description of any restrictions on data availability

The data that support the plots within this paper and other findings of this study are available from the corresponding author upon reasonable request.

Field-specific reporting

Please select the best fit for your research. If you are not sure, read the appropriate sections before making your selection.

☒ Life sciences ☐ Behavioural & social sciences ☐ Ecological, evolutionary & environmental sciences

For a reference copy of the document with all sections, see [nature.com/authors/policies/ReportingSummary-flat.pdf](https://www.nature.com/authors/policies/ReportingSummary-flat.pdf)

Life sciences study design

All studies must disclose on these points even when the disclosure is negative.

Sample size	the sample size for the parametric bootstrap (2000) and MCMC sampling (10 000 000) were chosen such that the estimated values remain constant upon further increase of the sample size
Data exclusions	no data were excluded
Replication	For the optimizations we used if possible a global solver (ANTIGONE) or repeated the optimization multiple times to ensure a global optimum.
Randomization	not relevant for this study
Blinding	not relevant for this study

Reporting for specific materials, systems and methods

Materials & experimental systems

n/a	Involved in the study
<input checked="" type="checkbox"/>	<input type="checkbox"/> Unique biological materials
<input checked="" type="checkbox"/>	<input type="checkbox"/> Antibodies
<input checked="" type="checkbox"/>	<input type="checkbox"/> Eukaryotic cell lines
<input checked="" type="checkbox"/>	<input type="checkbox"/> Palaeontology
<input checked="" type="checkbox"/>	<input type="checkbox"/> Animals and other organisms
<input checked="" type="checkbox"/>	<input type="checkbox"/> Human research participants

Methods

n/a	Involved in the study
<input checked="" type="checkbox"/>	<input type="checkbox"/> ChIP-seq
<input checked="" type="checkbox"/>	<input type="checkbox"/> Flow cytometry
<input checked="" type="checkbox"/>	<input type="checkbox"/> MRI-based neuroimaging